Isochrone overturning in steady glacier flow

Bradley Paul Lipovsky

Department of Earth and Space Sciences, University of Washington, Seattle, USA

Correspondence: bpl7@uw.edu
ORCID: https://orcid.org/0000-0003-4940-0745

Preprint status. This manuscript is a non-peer-reviewed preprint submitted to EarthArXiv. It has also been submitted to the *Journal of Glaciology*.

3 September 2026

Isochrone overturning in steady glacier flow

Bradley Paul LIPOVSKY

Department of Earth and Space Sciences, University of Washington, Seattle, USA

Correspondence: Bradley Paul Lipovsky, `bpl7@uw.edu`

ABSTRACT. Ancient ice recovered at Allan Hills extends into the Miocene, but steep layers, age reversals and folds complicate its interpretation. Whether steady glacier flow can overturn initially ordered layers remains uncertain. Here, we track the horizontal order of particles deposited sequentially at the surface. This order is measured by a signed Jacobian that is equivalent to the inverse vertical-thinning factor while layers remain ordered. We find that overturning depends directly on the cumulative competition between vertical shear, which preserves depositional order, and reverse shear, which erodes it. Reverse shear accumulates faster where horizontal speed is small. A layer becomes vertical only after reverse shear has erased both its initial ordering and the ordering accumulated during earlier flow. Full-Stokes mechanics does not guarantee preservation, although shallow-ice flow does. We derive an overturning threshold, bounds for localized obstacles, a cancellation result for periodic bed roughness and a trajectory-based diagnostic for numerical models. Gravity-driven full-Stokes flow with a linear sliding law generates recumbent folding directly from ordered surface deposition, without inherited disturbance or time dependence. Layer curvature and topographic draping can occur without order reversal; the Jacobian provides a test of steady-flow explanations of disturbed stratigraphy at Allan Hills and other old-ice sites.

Keywords: glacier flow; ice stratigraphy; recumbent folds; blue ice; full-Stokes modelling

INTRODUCTION

Recovering old ice is useful only where its age and stratigraphic context can be established. At Little Dome C, radar and flow modelling have been used to target a continuous record beyond 1 Ma (Lilien and others, 2021; Chung and others, 2025). Antarctic blue-ice areas instead expose discontinuous intervals through surface ablation and upward ice motion (Bintanja, 1999; Spaulding and others, 2012). The Sør Rondane Mountains are another blue-ice setting being surveyed for old ice (Izeboud and others, 2026). At Allan Hills, cores have progressed from disturbed ice near 1 Ma to Pliocene and Miocene ice and air approaching 6 Ma (Higgins and others, 2015; Yan and others, 2019; Shackleton and others, 2025).

Allan Hills ice is locally out of order: ALHIC1901 contains multiple age reversals (Shackleton and others, 2025); two recent cores have mean layer dips of approximately 29° and 69° (Kirkpatrick and others, 2025); and ALHIC1901 microstructure records simple shear, crystal-orientation stripes and centimetre-scale folds (Stoll and others, 2026). Radar and flow modelling show strong spatial variation in archive continuity and transport history (Kehrl and others, 2018; Manos and others, 2026). Layer deformation therefore affects the interpretation of the recovered ages.

It remains unclear whether fixed topography in a steady glacier can generate a recumbent fold. Flow over topography produces layer draping or overriding (Hindmarsh and others, 2006), while rough-bed Stokes solutions can contain local extrusion (i.e., faster flow at depth) or, at greater slopes, separated circulation (Gudmundsson, 1997a,b; Waddington, 2010). Whether these motions reverse stratigraphic order is less clear.

Observed basal folds motivated a distinction between initiation and passive amplification. Hudleston (1976) attributed Barnes Ice Cap folds to flow changes during minor advances or retreats, followed by bed-related shear. Whillans and Johnsen (1983) reproduced Byrd Station layer undulations using steady linear-viscous flow over basal variations, but did not obtain recumbent order reversal.

Airborne radar shows that order-reversing structures occur at ice-sheet scale. Dated horizons at Petermann Glacier contain overturned limbs and a sheath fold (Bons and others, 2016). Three-dimensional radar mapping in northeast Greenland resolved 500–600 m overturned anticline–syncline pairs associated with extinct ice streams (Franke and others, 2022). Franke and others (2022) interpreted these structures as upright folds formed by earlier convergent flow and subsequently sheared into recumbent geometries after flow reorganization.

Waddington and others (2001) examined whether local shear rotates a pre-existing wrinkle toward overturning or whether longitudinal extension flattens it, and argued that a transient process must first disturb steady stratigraphy. Finite-strain calculations later followed such inherited disturbances along trajectories and showed how divide migration can supply them (Jacobson and Waddington, 2004, 2005). For continuously generated steady stratigraphy, Parrenin and others (2006) introduced logarithmic flux coordinates, and Parrenin and Hindmarsh (2007) generalized this construction to horizontally non-uniform velocity. Their (π, θ) coordinates (see Table 1 for notation)—the logarithms of total flux and normalized streamfunction—make steady particle trajectories parallel straight lines labelled by their surface origin π_0. The associated path-sign parameter α measures the change in separation between neighboring surface origins and shows that an isochrone passes through vertical when $\alpha > 1$. They proved that upward-increasing horizontal velocity precludes this state, but did not construct a glacier flow with $\alpha > 1$ or connect the criterion to full-Stokes mechanics. Their framework also supports vertical thinning functions and numerical age solvers (Parrenin, 2013; Hindmarsh and others, 2009; Parrenin and others, 2025).

Steady accumulation and near-surface flow can produce single-valued firn undulations (Ng and King, 2011, 2013), whereas traveling basal-traction anomalies produce overturned folds through an explicitly transient mechanism (Wolovick and others, 2014; Wolovick and Creyts, 2016). Full-Stokes models also amplify seeded or active structures through anisotropy, basal shear and bed relief (Zhang and others, 2024). Not every fold-like radar return traces a continuous surface-deposited isochrone. Steep specular limbs may be poorly imaged (Holschuh and others, 2014), and some northern Greenland structures contain debris-rich horizons with diffuse scattering (Holschuh and others, 2026). The unresolved step is whether a steady glacier velocity field can overturn the passive age field generated continuously at the surface. Table 2 summarizes the relationship between these studies and the present analysis.

Here, we treat age as a passive, non-diffusive scalar introduced at surface deposition, and write the signed inverse vertical-thinning factor as the horizontal order of particles along an isochrone. Its cumulative budget separates surface-fast regular shear and extrusive reverse shear. We relate that budget to the full-Stokes stress balance, derive preservation regimes and obstacle bounds, and formulate a trajectory diagnostic. A gravity-driven full-Stokes example then overturns a surface-generated isochrone under a linear sliding law, without an inherited perturbation.

STEADY AGE TRANSPORT AND THE ORDER JACOBIAN

Kinematic coordinates and material origin

Let $u(x,z)$ and $w(x,z)$ be the horizontal and vertical components of a continuously differentiable, steady two-dimensional velocity field in a domain bounded above by $z = s(x)$. The flow is incompressible,

$$u_x + w_z = 0. \tag{1}$$

After orienting x downstream, horizontal velocity remains positive along every trajectory considered:

$$u(x,z) > 0. \tag{2}$$

Each trajectory intersects one upstream accumulation surface exactly once, at

$$x = x_0, \qquad z = s(x_0), \qquad \dot{a}(x_0) > 0, \tag{3}$$

where $\dot{a}$ is the ice-equivalent accumulation rate. Stratigraphic age is a passive, non-diffusive scalar that is zero at deposition and satisfies

$$\frac{\mathrm{D}\tau}{\mathrm{D}t} = \underbrace{\tau_t}_{=0} + u\tau_x + w\tau_z = u\tau_x + w\tau_z = 1, \qquad \tau = 0 \quad \text{at deposition.} \tag{4}$$

The Eulerian age field is steady, so $\tau_t = 0$, although the age of a moving particle increases at one unit of time per unit time.

Equations 1 and 4 give the age–streamfunction Jacobian identity below. Equation 2 permits integration in the downstream coordinate and excludes recirculation. Equation 3 assigns every trajectory a unique deposition coordinate x_0. Together they define a unique map from surface deposition to position on an isochrone and make the horizontal order Jacobian $\partial x/\partial x_0|_\tau$ well-defined. The discussion of steady overturning and limitations considers surface and basal sources, stagnation and other cases in which these conditions are not satisfied.

Equation 1 permits the velocity to be represented by a scalar streamfunction ψ. Curves of constant ψ are streamlines because $\boldsymbol{u} \cdot \nabla\psi = 0$, and the difference in ψ between two streamlines is their volume flux per unit width. The streamfunction is defined up to an arbitrary additive constant and requires no rheological assumption. We choose the orientation

$$u = \psi_z, \qquad w = -\psi_x. \tag{5}$$

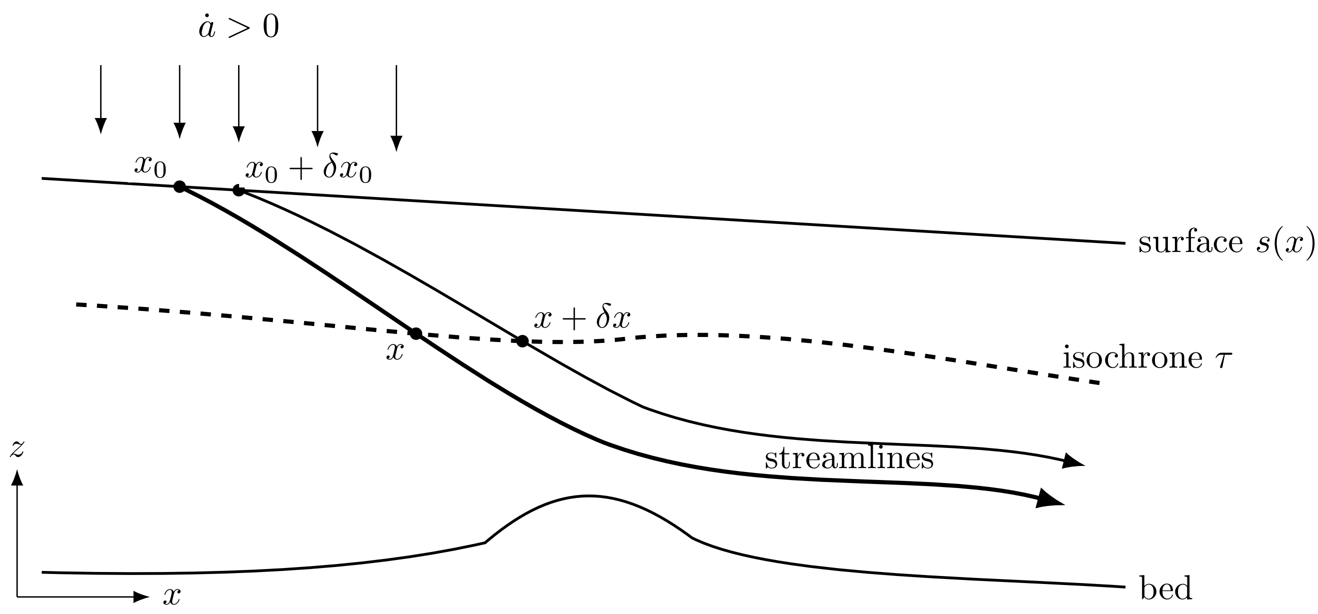

Figure 1. Material map for steady plane flow. Neighboring particles enter through the surface accumulation zone at x_0 and $x_0 + \delta x_0$, follow distinct streamlines and reach positions separated by δx at the same age τ. The order Jacobian is the limit of $\delta x/\delta x_0$. The curves enforce the kinematic requirements used in the derivation—surface origin, non-intersecting streamlines and transverse intersections with the isochrone—but are not a calculated Stokes solution.

Combining Equations 4 and 5 gives the exact Jacobian identity

$$\begin{vmatrix} \dfrac{\partial \tau}{\partial x} & \dfrac{\partial \tau}{\partial z} \\ \dfrac{\partial \psi}{\partial x} & \dfrac{\partial \psi}{\partial z} \end{vmatrix} = \tau_x \psi_z - \tau_z \psi_x = u\tau_x + w\tau_z = 1. \tag{6}$$

Thus age and streamfunction form local area-preserving coordinates. Isochrones and streamlines intersect transversely wherever the assumptions hold. Equivalently, (τ, ψ) are local canonical coordinates in the sense of Hamiltonian mechanics: ψ is the Hamiltonian for particle trajectories and $\{\tau, \psi\} = 1$. The inverse transformation directly measures stratigraphic order. The appendix on inverse-coordinate identities gives the relations used below. Figure 1 shows the deposition coordinate, two neighboring trajectories and their positions on an equal-age surface.

The streamfunction restricted to the surface is

$$\Psi(x) = \psi\big[x, s(x)\big]. \tag{7}$$

The steady surface kinematic condition is

$$u_s s_x - w\big|_{z=s(x)} = \dot{a}, \tag{8}$$

where $u_s = u\big[x, s(x)\big]$. Differentiating Ψ with the chain rule, substituting Equation 5, and then applying Equation 8 gives

$$\Psi'(x) = \psi_x|_{z=s(x)} + \psi_z|_{z=s(x)}\, s_x = -\, w|_{z=s(x)} + u_s s_x = \dot{a}(x) > 0. \tag{9}$$

The notation separates Eulerian position from material origin. The coordinate x is Eulerian: it identifies a fixed horizontal position in the steady velocity and age fields. The deposition coordinate x_0 is a material-origin label that remains associated with a particle as it moves, although x_0 alone labels a trajectory rather than a unique particle. At a specified age τ, x_0 parameterizes the particles on an isochrone and therefore serves as the Lagrangian coordinate used below.

The label x_0 is the physical-coordinate counterpart of the Parrenin–Hindmarsh coordinate π_0: both identify a particle by its surface origin. Retaining x_0 rather than transforming to logarithmic flux makes the present-day separation of neighboring origins directly measurable as a horizontal distance.

The streamfunction connects these descriptions. The increment $\mathrm{d}\psi$ is the ice flux per unit width between neighboring streamlines. At the surface, this flux is $\dot{a}_0\,\mathrm{d}x_0$, so larger accumulation places the same flux interval within a smaller deposition interval. Because $\Psi'(x) > 0$, every streamline label ψ has a unique deposition position $x_0(\psi)$ satisfying

$$\Psi(x_0) = \psi, \qquad \frac{\mathrm{d}x_0}{\mathrm{d}\psi} = \frac{1}{\dot{a}_0}, \tag{10}$$

where $\dot{a}_0 \equiv \dot{a}(x)|_{x=x_0} = \dot{a}(x_0)$ is the accumulation rate at deposition.

At fixed ψ, Equation 4 gives

$$\left.\frac{\partial \tau}{\partial x}\right|_{\psi} = \frac{1}{u}. \tag{11}$$

Consequently the age at (x, ψ) is the travel time from deposition. Here, ξ is the horizontal coordinate of integration and $z(\xi, \psi)$ is the elevation of the streamline labelled by ψ:

$$\tau(x, \psi) = \int_{x_0(\psi)}^{x} \frac{\mathrm{d}\xi}{u\,[\xi, z(\xi, \psi)]}. \tag{12}$$

At fixed x, Equation 5 implies

$$z_\psi = \frac{1}{u}. \tag{13}$$

Stratigraphic order compares travel times on neighboring streamlines, which are neighboring values of ψ. We therefore differentiate Equation 12 with respect to ψ at fixed downstream position. Using Equations 10 and 13 gives

$$\tau_\psi = -\frac{1}{\dot{a}_0 u_{s0}} - \int_{x_0}^{x} \frac{u_z}{u^3}\, \mathrm{d}\xi, \tag{14}$$

where $u_{s0} = u\,[x_0, s(x_0)]$ is the horizontal speed at deposition. The first term records the separation imposed at deposition; the integral records the subsequent differential travel time between neighboring streamlines.

Exact order theorem

The material-origin coordinate records whether an isochrone retains its depositional ordering. Curvature alone is insufficient because a strongly curved isochrone can remain a single-valued depth surface and preserve the sequence of particles established at deposition. At fixed age, increasing x_0 selects particles deposited successively farther downstream. Their order is preserved while their present horizontal position x also increases with x_0; a vertical tangent occurs when this horizontal separation vanishes, and overturning begins when its sign reverses.

Definition 1 (Isochrone-order Jacobian). The isochrone-order Jacobian is

$$\mathcal{J}(x, x_0) = \left.\frac{\partial x}{\partial x_0}\right|_\tau . \tag{15}$$

It measures whether particles deposited in increasing order of x_0 remain in increasing downstream order on an equal-age surface.

Theorem 1 (Cumulative order criterion). Under Equations 1–4, the isochrone-order Jacobian is

$$\boxed{\mathcal{J} = \frac{u(x,z)}{u_{s0}} \left(1 + \dot{a}_0 u_{s0} \int_{x_0}^{x} \frac{u_z}{u^3}\, \mathrm{d}\xi\right).} \tag{16}$$

It is also related exactly to the vertical age gradient by

$$\boxed{\mathcal{J} = -\dot{a}_0 \tau_z.} \tag{17}$$

Hence $\mathcal{J} > 0$ denotes ordered stratigraphy, $\mathcal{J} = 0$ a vertical tangent, and $\mathcal{J} < 0$ an overturned limb.

Proof. At fixed age, differentiation of $\tau(x, \psi)$ gives

$$\left.\frac{\partial x}{\partial \psi}\right|_\tau = -\frac{\tau_\psi}{\tau_x|_\psi} = -u\tau_\psi. \tag{18}$$

Multiplication by $\mathrm{d}\psi/\,\mathrm{d}x_0 = \dot{a}_0$ and substitution of Equation 14 gives Equation 16. At fixed x, $\tau_z = \tau_\psi \psi_z = u\tau_\psi$, which gives Equation 17. □

The correction of annual-layer thickness for cumulative ice deformation goes back at least to Nye (1963) and Dansgaard and Johnsen (1969). In the present notation, the vertical thinning function λ_z is the current vertical thickness of an infinitesimal age layer divided by its ice-equivalent thickness at deposition. For an ordered layer, a positive age increment $\mathrm{d}\tau$ corresponds to the present vertical thickness $-\,\mathrm{d}z = -\,\mathrm{d}\tau/\tau_z$ and the initial thickness $\dot{a}_0\,\mathrm{d}\tau$. Hence

$$\boxed{\lambda_z = -\frac{1}{\dot{a}_0\tau_z} = \mathcal{J}^{-1}, \qquad \mathcal{J} > 0.} \tag{19}$$

In ordered stratigraphy, $\mathcal{J}$ is the inverse of the established vertical thinning function (Parrenin, 2013; Parrenin and others, 2025). Equation 17 continues this measure with a sign through a vertical tangent. The positive thinning function diverges as $\tau_z \to 0$, whereas $\mathcal{J}$ crosses zero regularly and records orientation reversal.

At deposition, $x = x_0$, $u = u_{s0}$, and $\mathcal{J} = 1$. At the first vertical tangent, $\tau_z = 0$, but the material curve remains regular. Inverting Equation 6 shows that

$$\left.\frac{\partial z}{\partial x_0}\right|_\tau = \dot{a}_0\tau_x. \tag{20}$$

When $\mathcal{J} = 0$, Equation 4 gives $\tau_x = 1/u$, and therefore

$$\left.\frac{\partial z}{\partial x_0}\right|_{\tau,\mathcal{J}=0} = \frac{\dot{a}_0}{u} > 0. \tag{21}$$

The divergence of the conventional slope $m = \mathrm{d}z/\,\mathrm{d}x$ at overturning is therefore a coordinate singularity, not a singularity of the layer itself.

Positive and reverse shear budgets

Define

$$u_z^+ = \max(u_z, 0), \qquad u_z^- = \max(-u_z, 0), \tag{22}$$

and the dimensionless cumulative contributions

$$\mathcal{P}(x, x_0) = \dot{a}_0 u_{s0} \int_{x_0}^{x} \frac{u_z^+}{u^3}\,\mathrm{d}\xi, \tag{23}$$

$$\mathcal{R}(x, x_0) = \dot{a}_0 u_{s0} \int_{x_0}^{x} \frac{u_z^-}{u^3}\,\mathrm{d}\xi. \tag{24}$$

Equation 16 becomes

$$\boxed{\mathcal{J} = \frac{u}{u_{s0}}\mathcal{B}, \qquad \mathcal{B} \equiv 1 + \mathcal{P} - \mathcal{R}.} \tag{25}$$

The dimensionless factor $\mathcal{B}$ is an order budget: deposition contributes the initial value one, normal shear adds $\mathcal{P}$, and reverse shear subtracts $\mathcal{R}$. Because $u/u_{s0} > 0$, the necessary-and-sufficient condition for preservation of horizontal order is

$$\boxed{\mathcal{R} < 1 + \mathcal{P}.} \tag{26}$$

The first vertical tangent occurs at

$$\boxed{\mathcal{R} = 1 + \mathcal{P},} \tag{27}$$

and overturning occurs when $\mathcal{R} > 1 + \mathcal{P}$.

The unit term in Equations 25–27 represents the initial ordering imposed at deposition. Positive u_z, the usual surface-fast glacier profile, adds to the budget. Reverse shear must remove both contributions. Thus a local region with $u_z < 0$ is not itself a fold criterion.

In travel-time coordinates, $\mathrm{d}x = u\ \mathrm{d}t$, so

$$\mathcal{R} = \dot{a}_0 u_{s0} \int_0^T \frac{u_z^-}{u^2}\ \mathrm{d}t. \tag{28}$$

where T is the travel time from deposition to the point of interest. The contribution of reverse shear grows with residence time and as horizontal speed decreases. Local extrusion in fast throughflow may therefore leave stratigraphic order unchanged, while modest reverse shear near stagnation can dominate the order budget.

Corollary 1 (Monotonic-shear result). If $u_z \geq 0$ everywhere along a trajectory, then $\mathcal{R} = 0$, $\mathcal{J} > 0$, and the steady isochrone cannot overturn.

This corollary is the physical-coordinate statement of the no-overturning result in Appendix A of Parrenin and Hindmarsh (2007). Finite intervals of reverse shear also preserve order when their cumulative weighted contribution remains below the budget in Equation 26. Figure 2 summarizes the three contributions and the point at which the budget reaches zero.

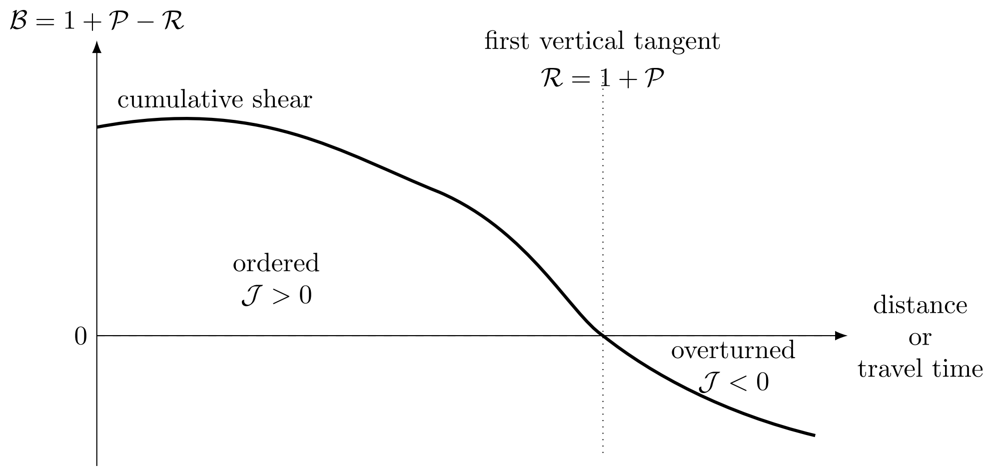

Figure 2. Conceptual order budget. The sign of $\mathcal{B} = 1 + \mathcal{P} - \mathcal{R}$ is the sign of the order Jacobian. Local reverse shear need not cause overturning; a vertical tangent appears only after cumulative reverse shear removes the initial depositional contribution and the accumulated normal-shear contribution.

Relation to the Parrenin–Hindmarsh (π, θ) coordinates

In the notation of Parrenin and Hindmarsh (2007), $Q(x)$ is total horizontal flux and Ω is the streamfunction normalized by Q. They defined

$$\pi = \ln\left[\frac{Q(x)}{Q^{\mathrm{ref}}}\right], \qquad \theta = \ln\Omega. \tag{29}$$

Steady trajectories satisfy $\mathrm{d}\theta/\,\mathrm{d}\pi = -1$, and hence $\theta = \pi_0 - \pi$. Curved trajectories in physical space therefore become parallel straight lines labelled by the deposition coordinate π_0. For two neighboring particles, their Appendix A gives

$$\delta\pi = (1-\alpha)\,\delta\pi_0, \tag{30}$$

where the path-sign parameter α accumulates changes in the velocity profile along the trajectory. Thus $1-\alpha$ is the signed deformation of neighboring surface origins in logarithmic flux coordinates, and an isochrone exceeds vertical when $\alpha > 1$. Their present and surface-origin coordinates are monotone functions of x and x_0 wherever Equations 2 and 3 hold. Consequently,

$$\operatorname{sgn}(1-\alpha) = \operatorname{sgn}\left(\left.\frac{\partial x}{\partial x_0}\right|_{\tau}\right) = \operatorname{sgn}(\mathcal{J}) = \operatorname{sgn}(-\tau_z). \tag{31}$$

The order Jacobian carries the same sign information as $1-\alpha$, and Equation 19 identifies it as the signed inverse vertical-thinning factor. In physical space, it separates the positive and negative parts of vertical shear, remains regular at the first vertical tangent and can be evaluated directly from a numerical velocity field.

FULL-STOKES CONSTRAINTS ON ISOCHRONE ORDER

Exact stress decomposition of vertical shear

The order theorem applies to any velocity field satisfying the preceding kinematic equations. For steady, isothermal or thermomechanically prescribed, isotropic generalized-Newtonian Stokes flow, the momentum and constitutive equations constrain the vertical shear:

$$\nabla \cdot \boldsymbol{u} = 0, \tag{32}$$

$$-\nabla p + \nabla \cdot \boldsymbol{\tau} + \rho \boldsymbol{g} = \boldsymbol{0}, \tag{33}$$

$$\boldsymbol{\tau} = 2\eta \boldsymbol{D}, \qquad \boldsymbol{D} = \tfrac{1}{2}\left(\nabla \boldsymbol{u} + \nabla \boldsymbol{u}^{\mathsf{T}}\right), \qquad \eta > 0. \tag{34}$$

Here, p is pressure, ρ is ice density, $\boldsymbol{g}$ is gravitational acceleration, $\boldsymbol{\tau}$ is deviatoric stress, $\boldsymbol{D}$ is the strain-rate tensor and $\eta > 0$ is the scalar effective viscosity. The viscosity may depend on temperature and effective strain rate. Anisotropic rheology is discussed separately below.

With z vertical and gravity having no horizontal component, the horizontal momentum equation is

$$-p_x + \tau_{xx,x} + \tau_{xz,z} = 0. \tag{35}$$

Write

$$p = p_{\mathrm{atm}} + \rho g(s - z) + p_{\mathrm{nh}}, \tag{36}$$

where $g = |\boldsymbol{g}|$, p_{atm} is atmospheric pressure and p_{nh} contains all nonhydrostatic pressure, including the finite-slope surface correction. Integrating Equation 35 downward from the free surface, with ζ as the vertical coordinate of integration, gives

$$\tau_{xz}(x, z) = \tau_{xz}^{s} - \rho g s_x (s - z) + \int_z^s \left(\tau_{xx,x} - p_{\mathrm{nh},x}\right) \mathrm{d}\zeta. \tag{37}$$

Because $\tau_{xz} = \eta(u_z + w_x)$,

$$\boxed{u_z = \underbrace{\frac{\rho g(s - z)(-s_x)}{\eta}}_{G} + \underbrace{\left[-w_x + \frac{\tau_{xz}^{s}}{\eta} + \frac{1}{\eta}\int_z^s \left(\tau_{xx,x} - p_{\mathrm{nh},x}\right) \mathrm{d}\zeta\right]}_{R_{\mathrm{FS}}}.} \tag{38}$$

where the superscript s denotes surface stress. For a surface descending downstream, $s_x \leq 0$, the gravity-driven term G is nonnegative and favors order preservation. The residual R_{FS} contains the full-Stokes effects omitted from the shallow-ice shear balance: gradients of vertical velocity, longitudinal stress, nonhydrostatic pressure and the Cartesian surface shear-stress component.

Substitution into Equation 16 gives

$$\mathcal{J} = \frac{u}{u_{s0}} \left(1 + \mathcal{G} + \mathcal{F}\right), \tag{39}$$

with

$$\mathcal{G} = \dot{a}_0 u_{s0} \int_{x_0}^{x} \frac{G}{u^3}\, \mathrm{d}\xi \geq 0, \tag{40}$$

$$\mathcal{F} = \dot{a}_0 u_{s0} \int_{x_0}^{x} \frac{R_{\mathrm{FS}}}{u^3}\, \mathrm{d}\xi. \tag{41}$$

The exact full-Stokes condition for a vertical or overturned isochrone is

$$\boxed{\mathcal{F} \leq -\left(1 + \mathcal{G}\right).} \tag{42}$$

A conservative sufficient condition for no overturning is

$$\boxed{\dot{a}_0 u_{s0} \int_{x_0}^{x} \frac{[R_{\mathrm{FS}}]_-}{u^3}\, \mathrm{d}\xi < 1.} \tag{43}$$

This conservative bound is easy to test because it discards all positive contributions, including gravity-driven shear.

Full-Stokes mechanics permits reverse shear

Neither incompressibility nor the Stokes equations fixes the sign of u_z. The constitutive relation constrains $u_z + w_x$, while longitudinal stress and nonhydrostatic pressure can alter the Cartesian vertical gradient of horizontal speed. Analytical rough-bed solutions predict local velocity maxima and minima, and therefore regions with $u_z < 0$, even for gravity-driven linear viscous flow (Gudmundsson, 1997a). The historical extrusion-flow literature likewise shows that surface-fast velocity profiles are not a pointwise theorem of full-Stokes mechanics (Waddington, 2010).

At stronger roughness, the one-way-flow assumption itself can fail. Gudmundsson (1997b) found separated secondary circulation in troughs of sufficiently steep sinusoidal beds. Moffatt (1964) considered the local similarity solution near a sharp corner. For two stationary rigid planes, the similarity exponent becomes complex when the included angle is less than approximately 146°; the resulting oscillation with logarithmic radial distance gives a nested sequence of closed, counter-rotating streamlines. Meyer and Creyts (2017) extended this corner-flow mechanism to Glen-law ice in subglacial mountain valleys and showed that oblique flow can produce three-dimensional eddies.

Moffatt eddies require a recirculating corner-flow mode, whereas isochrone overturning under Equations 1–4 requires the order budget along an open trajectory to reach zero. The circular-arc bed calculation in Figure 3 overturns with $u > 0$ along every plotted trajectory, so a Moffatt eddy is not necessary. A closed streamline is incompatible with the steady, surface-sourced age field: integrating Equation 4 around an orbit of period $T > 0$ would give

$$\tau(T) - \tau(0) = \int_0^T \frac{\mathrm{D}\tau}{\mathrm{D}t}\,\mathrm{d}t = T,$$

although return to the same point requires $\tau(T) = \tau(0)$. A Moffatt eddy may deform inherited layers or contain ice supplied by another boundary, but it cannot contain the steady surface-sourced age field considered here.

Published rough-bed solutions show that u_z can be negative. Order reversal further requires the integrated reverse-shear contribution $\mathcal{R}$ to reach $1 + \mathcal{P}$.

REGIMES THAT PRESERVE ORDER

Shallow-ice flow

Under the conventional shallow-ice approximation,

$$\tau_{xz} \simeq -\rho g(s - z)s_x. \tag{44}$$

For downstream flow with $s_x < 0$, $\tau_{xz} > 0$. An isotropic Glen-type rheology gives u_z with the same sign as τ_{xz}, while leading-order basal sliding contributes a depth-independent horizontal speed (Cuffey and Paterson, 2010). Therefore

$$u_z \geq 0, \qquad \mathcal{R} = 0, \qquad \mathcal{J} > 0. \tag{45}$$

A fixed bed obstacle can produce arches, troughs and finite curvature in shallow-ice stratigraphy, but it cannot overturn a steady isochrone under these assumptions.

Regular thin-film full-Stokes flow

Let

$$\varepsilon = \frac{H}{L} \ll 1 \tag{46}$$

be the aspect ratio of a smooth glacier. Higher-order glacier models reproduce the Stokes solution to second order in ε under their regular asymptotic assumptions, including a range of basal slip regimes (Blatter, 1995; Schoof and Hindmarsh, 2010). Suppose the non-shallow contribution scales as

$$R_{\mathrm{FS}} = O\left(\varepsilon^2 \frac{U}{H}\right) \tag{47}$$

through a region of length $L = H/\varepsilon$, and suppose u remains comparable to U. Then

$$\mathcal{F} = O\left(\frac{\dot{a}}{U}\varepsilon\right). \tag{48}$$

Thus small regular full-Stokes corrections cannot erase the initial depositional contribution when

$$\frac{\dot{a}}{U}\varepsilon \ll 1. \tag{49}$$

This asymptotic regime excludes divides, abrupt sliding transitions, contact zones, steep obstacles, very slow flow and other regions where the thin-film expansion is singular or nonuniform.

A sufficient bound for a localized obstacle

The cumulative criterion bounds the effect of a localized obstacle without requiring pointwise monotonic shear.

Proposition 1 (Localized reverse-shear bound). Suppose reverse shear is confined to a trajectory segment of horizontal length ℓ. On that segment, assume

$$u \geq U_{\min} > 0, \qquad u_{s0} \leq U_{\mathrm{dep}}, \qquad u_z^- \leq \dot{\gamma}_{\mathrm{rev}}, \tag{50}$$

where $U_{\min}$ is the minimum horizontal speed on the segment, U_{dep} bounds the horizontal speed at deposition, and $\dot{\gamma}_{\mathrm{rev}}$ bounds the reverse vertical shear rate. Then

$$\boxed{\mathcal{R} \leq \frac{\dot{a}_0 U_{\mathrm{dep}} \dot{\gamma}_{\mathrm{rev}} \ell}{U_{\min}^3}.} \tag{51}$$

A sufficient condition for no overturning is that the right-hand side be less than one.

Proof. Substitute Equation 50 into Equation 24 and bound the integral by its maximum integrand multiplied by ℓ. □

For an isolated obstacle whose horizontal and vertical influence scales are both $O(H)$, with non-stagnant throughflow,

$$\mathcal{R} = O\left(\frac{\dot{a}}{U}\right). \tag{52}$$

In a typical interior or flank setting where $U \gg \dot{a}$, an isolated fixed bump can create local extrusion and visible draping while remaining far from the reverse-shear value required for a vertical tangent. More generally, setting the right-hand side of Equation 51 equal to one and solving for length gives

$$\ell \gtrsim \frac{U_{\mathrm{min}}^3}{\dot{a}_0 U_{\mathrm{dep}} \dot{\gamma}_{\mathrm{rev}}}. \tag{53}$$

Slow throughflow reduces this required length through the U_{min}^3 numerator. For scale, take $\dot{a}_0 = 0.05\ \mathrm{m\,yr^{-1}}$, $U_{\mathrm{dep}} = 10\ \mathrm{m\,yr^{-1}}$, $\dot{\gamma}_{\mathrm{rev}} = 0.01\ \mathrm{yr^{-1}}$ and $\ell = 1$ km. Equation 51 gives $\mathcal{R} \leq 0.005$ when $U_{\mathrm{min}} = 10\ \mathrm{m\,yr^{-1}}$, which rules out overturning under these assumed bounds. With $U_{\mathrm{min}} = 1\ \mathrm{m\,yr^{-1}}$, the bound is $\mathcal{R} \leq 5$ and no longer rules it out.

For non-stagnant flow, localized deformation and a small accumulation-to-speed ratio, Equation 51 explains why flow over an isolated bump commonly preserves isochrone order.

First-order cancellation over periodic roughness about plug flow

Fixed periodic roughness can also have weak cumulative effect through cancellation about a plug-flow background. Let

$$u(x, z; \epsilon_b) = U_b + \epsilon_b u_1(x, z) + O(\epsilon_b^2), \qquad U_b > 0, \tag{54}$$

where ϵ_b is a small amplitude parameter, $U_b > 0$ is spatially uniform, u_1 is periodic in x, and k is its wavenumber. The perturbation has wavelength $2\pi/k$ and zero horizontal mean at each elevation. Along the unperturbed trajectory $z = z_0$,

$$\frac{u_z}{u^3} = \epsilon_b \frac{u_{1,z}(x, z_0)}{U_b^3} + O(\epsilon_b^2). \tag{55}$$

Therefore, over one complete wavelength,

$$\int_x^{x+2\pi/k} \frac{u_z}{u^3}\ \mathrm{d}\xi = O(\epsilon_b^2). \tag{56}$$

The appendix on first-order periodic cancellation gives the expansion leading to Equation 56. The perturbative frictionless rough-bed solution of Gudmundsson (1997a) has this plug-flow structure: local extrusion occurs, but its first-order stoss- and lee-side contributions cancel over a complete symmetric wavelength.

The first-order cancellation in Equation 56 does not apply to a sheared background, a solitary asymmetric obstacle, a finite path ending mid-cycle, strongly nonlinear roughness or near-stagnant trajectories.

TRAJECTORY DIAGNOSTIC FOR FULL-STOKES MODELS

The order criterion can be evaluated without explicitly solving the age equation or advecting a dense family of isochrones. Start trajectories in a surface accumulation zone and record x_0, $\dot{a}_0$ and u_{s0}. With t denoting time since deposition, integrate along each trajectory

$$\frac{\mathrm{d}x}{\mathrm{d}t} = u, \qquad \frac{\mathrm{d}z}{\mathrm{d}t} = w, \tag{57}$$

$$\frac{\mathrm{d}\mathcal{P}}{\mathrm{d}t} = \dot{a}_0 u_{s0}\frac{u_z^+}{u^2}, \qquad \frac{\mathrm{d}\mathcal{R}}{\mathrm{d}t} = \dot{a}_0 u_{s0}\frac{u_z^-}{u^2}, \tag{58}$$

with $\mathcal{P}(0) = \mathcal{R}(0) = 0$. Then

$$\boxed{\mathcal{J}(t) = \frac{u(t)}{u_{s0}}\left[1 + \mathcal{P}(t) - \mathcal{R}(t)\right].} \tag{59}$$

The diagnostic is

$$\min_t \left[1 + \mathcal{P}(t) - \mathcal{R}(t)\right] \begin{cases} > 0, & \text{order preserved,} \\ = 0, & \text{first vertical tangent,} \\ < 0, & \text{overturned steady isochrone.} \end{cases} \tag{60}$$

A robust implementation should include four checks. First, compare Equation 59 with $-\dot{a}_0\tau_z$ from an independently solved steady age equation. Second, advect at least one pair of neighboring particles to verify the sign of $\partial x/\partial x_0|_\tau$. Third, stop the downstream-coordinate integration when u approaches zero and diagnose recirculation with the full trajectory topology. Fourth, compute u_z using the finite-element gradient rather than differencing noisy interpolated velocities. Separate storage of $\mathcal{P}$ and $\mathcal{R}$ is preferable to integrating their difference because large compensating contributions can otherwise obscure numerical error.

For transient flow, Equation 59 is not valid because the steady travel-time representation fails. The corresponding calculation should integrate the deformation of the two-parameter deposition map through time. Nevertheless, the steady order budget remains useful as a baseline and as a diagnostic applied to quasi-steady snapshots.

FULL-STOKES NUMERICAL EXAMPLE

We construct an idealized steady full-Stokes flow that generates a recumbent fold from ordered surface deposition without an imposed internal disturbance. Gravity drives the flow, and the bed obeys a linear sliding law. The model is not a reconstruction of Allan Hills or another old-ice site.

The two-dimensional domain has a flat upper surface and a bed whose vertical cross section is a circular arc of radius 250 m. Its maximum thickness is 150 m, and it is truncated by vertical cuts where the ice has positive thickness. Ice is incompressible and linear viscous, with $\eta = 2.5 \times 10^8$ Pa yr and $\rho = 917$ kg m^{-3}. Gravity acts at a mean surface slope of 0.05 rad. We implemented the weak form in Firedrake version `0.13.0+11207.g7ed6ff028`, generated curved unstructured meshes with Gmsh, imposed basal impermeability with symmetric Nitsche terms and solved the mixed system with the MUMPS direct solver. Velocity and pressure use Taylor–Hood elements, with quadratic velocity and linear pressure.

During model development, OpenAI `5.6-sol` was used to search candidate boundary conditions, including bed geometry, for a clear example of steady overturning. The final geometry and boundary conditions were then evaluated using the governing equations, mechanical power balance, trajectory topology and mesh-refinement tests reported here.

The bed is impermeable and obeys the linear sliding law

$$u_t = C\tau_b, \qquad u_n = 0, \qquad \tau_b = -\boldsymbol{t} \cdot \boldsymbol{\sigma} \boldsymbol{n}, \tag{61}$$

where u_t and u_n are the tangential and normal basal velocities, $\boldsymbol{t}$ and $\boldsymbol{n}$ are the bed tangent and outward normal, $\boldsymbol{\sigma}$ is the full Cauchy stress, τ_b is the resisting basal shear stress, and $C = 10^{-5}$ m yr^{-1} Pa^{-1} is the mobility. Because $C > 0$, Equation 61 dissipates mechanical energy. The surface is traction free. Each lateral boundary has the hydrostatic traction $-\rho g \cos\beta(-z)\boldsymbol{n}$, where β is the mean surface slope. The accumulation rate required to keep the surface fixed is diagnosed as $\dot{a} = -\left. w\right|_{z=0}$, and particles are introduced only where $\dot{a} > 0$.

The numerical isochrones are generated from the deposition boundary. At age zero, a particle labelled by x_0 is placed at $[x_0, 0]^\mathsf{T}$. Integrating the steady velocity for a common age τ gives the material curve $[x(x_0, \tau), z(x_0, \tau)]^\mathsf{T}$. No internal layer, wrinkle or fold is initialized. A negative value of $\partial x/\partial x_0|_\tau$ therefore measures order reversal generated between deposition and the plotted isochrone.

For the representative calculation, the ice is 70 m thick at both lateral boundaries. The boundaries together remove 4.3×10^2 Pa m^2 yr^{-1} of mechanical power per unit width, whereas gravity supplies

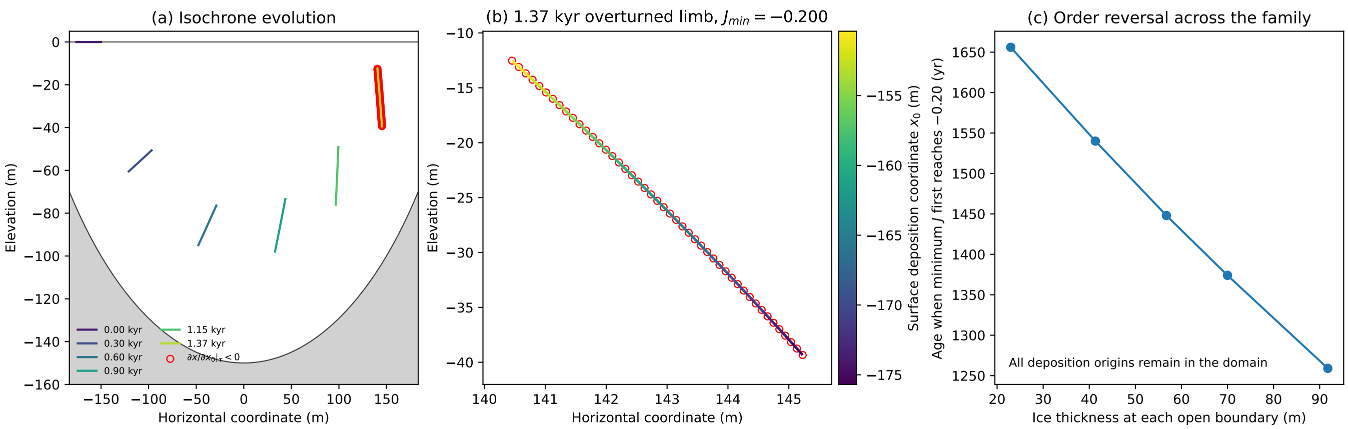

Figure 3. Gravity-driven order reversal with positive thickness at both lateral boundaries. The bed cross section is a circular arc with 150 m maximum ice thickness, and the bed obeys a linear sliding law; hydrostatic traction is applied on the open lateral cuts. (a) Isochrone evolution at 0, 0.30, 0.60, 0.90, 1.15 and 1.374 kyr, for 70 m boundary thickness. Each curve consists of the same surface-deposition origins evaluated at a common age. (b) Detail at the final age, when the minimum order Jacobian is less than −0.20. Color gives deposition coordinate x_0, and open red circles mark $\mathcal{J} < 0$. (c) Age at which the same threshold is crossed as boundary thickness increases from 23 to 92 m. All deposition origins remain in the domain at the plotted threshold.

4.63×10^6 $\mathrm{Pa\,m^2\,yr^{-1}}$. The lateral tractions therefore do not drive the flow. The deposition map first reaches $\mathcal{J} = -0.20$ at 1.374 kyr (Figure 3a–b). At that age, all 47 surface origins spanning 25.9 m remain within the domain, and horizontal speed has remained above 0.143 $\mathrm{m\,yr^{-1}}$. The same threshold is reached with 23–92 m of ice at both boundaries (Figure 3c).

Horizontal speed remains positive along every plotted trajectory, so the streamlines are open and exclude a Moffatt eddy. Reverse shear rotates the surface-deposition map through vertical while the lateral ice thickness remains positive.

For the 70 m boundary-thickness case, meshes with nominal spacings of 15, 10, 7.5 and 5 m give $\mathcal{J} = -0.20061$, -0.20053, -0.20040 and -0.20037, respectively, at the first resolved threshold. The overturned interval and its age are therefore insensitive to mesh refinement at the reported precision.

The topographic relief is large and the rheology is linear viscous. This idealized calculation gives a gravity-driven flow with a linear sliding law and positive lateral thickness that overturns a surface-generated isochrone. Testing the mechanism at Allan Hills requires measured three-dimensional geometry, a basal traction model and source-to-core trajectories consistent with the observed surface mass balance.

DISCUSSION

Limits of the steady coordinate construction

For flow satisfying Equations 1–4, cumulative reverse shear can overturn an isochrone when Equation 27 is met, without a change in boundary conditions. The extrusion-flow literature describes local reverse shear without evaluating this cumulative threshold. Variable density requires the mass-flux extension given in the appendix.

Stagnation and recirculation instead violate the coordinate construction. If u vanishes or reverses, downstream position no longer parameterizes a trajectory and the $1/u$ and $1/u^3$ integrals become singular. Time integration remains possible, but a closed streamline cannot have the unique surface origin assumed here. The Allan Hills model of Manos and others (2026) approaches this limit: its near-stagnant basal flow remains nonzero, yet makes the order integral sensitive to small velocities.

Material sources also restrict the theorem. A trajectory may enter through accumulation and leave through surface ablation, but its deposition coordinate must be defined on the originating accumulation zone. Multiple surface sources or basal freeze-on require a more general label. Basal melting and ablation truncate layers, while freeze-on can add debris-bearing structures that are not surface-deposited isochrones (Leysinger Vieli and others, 2018; Holschuh and others, 2026).

Changes in geometry or basal traction leave an inherited age field that differs from the steady age solution. Divide migration, traveling traction anomalies and former ice-stream configurations can therefore seed folds later amplified by shear (Jacobel and Bindschadler, 1993; Jacobson and Waddington, 2005; Wolovick and others, 2014; Wolovick and Creyts, 2016; Franke and others, 2022; Jansen and others, 2024). These mechanisms remain distinct from overturning generated continuously in a fixed velocity field.

Finally, Equation 38 assumes isotropic scalar viscosity and the order theorem is two-dimensional. Fabric and rheological heterogeneity can actively generate folds (Alley and others, 1997; Thorsteinsson and Waddington, 2002; Bons and others, 2016, 2025), and convergent anisotropic flow occurs in both radar observations and models (Ross and others, 2020; Martín and others, 2009). In three dimensions, the relevant quantity is the two-dimensional Jacobian mapping a surface deposition patch to an equal-age surface. The scalar $\mathcal{J}$ applies only within a coherent flow tube with negligible cross-flow.

Implications for old-ice sites

Allan Hills approaches several limits of the two-dimensional calculation. Ice rises into an ablation zone above steep nunatak topography (Spaulding and others, 2012; Kehrl and others, 2018; Stoll and others, 2026).

Manos and others (2026) predict nearly stagnant basal ice upstream of the nunatak: the bottom 20 m averages 0.4–0.5 $\mathrm{mm\,yr^{-1}}$, with local speeds of order micrometres per year, compared with 46–49 $\mathrm{mm\,yr^{-1}}$ in the Cul-de-sac. Such small u makes the u^{-3} order integral numerically sensitive. The modeled flow is also three-dimensional, with bridging stresses represented in two dimensions by the $-w_x$ term in Equation 38. Finally, Cul-de-sac transport and geochemistry indicate a distinct accumulation environment. A three-dimensional, multi-source material map is therefore required there.

Observations constrain but do not determine this history. The 69° mean dip in ALHIC2302 remains below vertical (Kirkpatrick and others, 2025), and centimetre-scale folds in ALHIC1901 need not explain core-scale reversals (Stoll and others, 2026). The ALHIC1901 age–depth inversion implies $\mathcal{J} < 0$ through Equation 17 only if samples belong to one continuous surface-deposited layer family (Shackleton and others, 2025).

At Little Dome C, radar and flow modelling indicate strong basal thinning and possibly stagnant or disturbed ice (Lilien and others, 2021; Chung and others, 2025). Evaluating $\mathcal{J}$ along trajectories would test whether steady flow preserves order above this basal unit.

The equations suggest four tests of an observed fold or age reversal.

(1) **Steady geometry.** Evaluate $\mathcal{P}$, $\mathcal{R}$ and $\mathcal{J}$ along source-to-core trajectories. A positive budget excludes steady overturning.

(2) **Flow topology and sources.** Test for stagnation, recirculation, freeze-on and multiple surface origins; these require the full material map.

(3) **Unsteady inheritance.** If steady flow preserves order, evaluate past changes in geometry, ablation and basal traction.

(4) **Active deformation.** If passive models underpredict folding, couple fabric and rheological heterogeneity to flow.

In regular, shallow, non-stagnant flow, Equation 51 favors a time-dependent or rheological mechanism. More general full-Stokes flow can overturn steady isochrones if reverse shear crosses the order threshold.

Novelty and relationship to established theory

Studies of folding in rocks provide a useful comparison. Competence contrasts can drive active buckling, whereas passive layers record heterogeneous flow imposed by their surroundings; both processes can produce recumbent or sheath folds (Bastida and others, 2014; Schmalholz and Mancktelow, 2016; Nabavi and Fossen, 2021). Recent fabric and field studies further show that similar sheath folds can reflect early active folding, later passive amplification, fold-axis rotation or a combination of these processes (Fazio and others, 2024;

Alsop and Condon, 2025). These studies generally describe the finite deformation of pre-existing layers. Here, isochrones are instead generated continuously at deposition, and we ask whether fixed steady flow can reverse that initially ordered map without an inherited disturbance or rheological contrast.

The analysis builds most directly on the Parrenin–Hindmarsh (π, θ) coordinates, path-sign factor and monotonic-shear result (Parrenin and others, 2006; Parrenin and Hindmarsh, 2007). It also uses established material-line kinematics (Waddington and others, 2001), finite-strain amplification (Jacobson and Waddington, 2004), vertical thinning (Parrenin, 2013; Parrenin and others, 2025) and rough-bed extrusion (Gudmundsson, 1997a). In physical space, the signed flux-coordinate mapping becomes a positive–negative u_z/u^3 budget from which the full-Stokes residual threshold, localized-obstacle bound, periodic cancellation result and trajectory diagnostic follow.

Parrenin and others (2006) represented the horizontal velocity profile using a prescribed shape function of normalized depth, a separable approximation that enabled an analytical age solution. Their coordinate construction is more general than this profile. Here, the order theorem admits a general steady two-dimensional velocity field, and the full-Stokes momentum and constitutive equations determine the reverse shear that enters the order budget.

We are not aware of a previous full-Stokes calculation in which a time-independent glacier velocity carries an ordered surface-deposition map to $\mathcal{J} < 0$ without an internal wrinkle. In the present example, gravity drives the flow, a linear sliding law dissipates energy, lateral tractions are hydrostatic, and both lateral ice thickness and trajectory speed remain positive. The circular-arc bed provides an idealized geometry for this mechanism.

Applying the diagnostic to reconstructed Allan Hills flow would distinguish a positive budget, which excludes steady overturning, from a trajectory crossing $\mathcal{J} = 0$. Layer attitudes, age reversals and fabric provide independent tests.

Limitations

The analysis assumes a smooth two-dimensional velocity, isotropic scalar viscosity and one surface origin per trajectory. The obstacle bound requires externally supplied velocity and shear bounds, while periodic cancellation is only first order. The Jacobian $\mathcal{J}$ diagnoses only a continuous material isochrone. Faults, unconformities, freeze-on, multiple sources and unresolved three-dimensional geometry can also produce apparent age reversals. Steep specular limbs or debris-rich diffuse reflectors add ambiguity in radar data (Holschuh and others, 2014, 2026).

CONCLUSIONS

The signed order Jacobian measures depositional order in a steady two-dimensional isochrone (Equation 16). It is observable as $-\dot{a}_0\tau_z$ (Equation 17) and, while positive, is the reciprocal of the established vertical thinning function (Equation 19). The order budget separates the initial and normal-shear contributions from cumulative reverse shear; overturning begins when $\mathcal{R} = 1 + \mathcal{P}$ (Equation 27).

Full-Stokes mechanics permits reverse shear through longitudinal stress, nonhydrostatic pressure and horizontal gradients of vertical velocity (cf. Equation 38). Shallow-ice flow preserves order (Equation 45), while localized obstacles and small-amplitude periodic roughness preserve it under the bounds in Equations 51 and 56. Stagnation and recirculation invalidate the one-way coordinate construction.

The numerical example generates a recumbent isochrone directly from ordered surface deposition (Figure 3). Gravity drives the flow, the bed obeys a linear sliding law, and both lateral ice thickness and horizontal velocity along the relevant trajectories remain positive. This steady full-Stokes flow crosses the order threshold under glaciological boundary conditions.

The order budget at old ice sites provides a common test of whether local flow preserves deposition order. Applying it requires reconstructed trajectories and, where cross-flow or multiple source regions are important, a three-dimensional material map. A fold complicates a climate archive, but it also preserves a mechanical record of the flow that brought ancient ice within reach.

DATA AVAILABILITY STATEMENT

No new observational data are presented. The analytical results are fully specified by the equations in this manuscript. Executed notebooks contain the full-Stokes solves, trajectory calculations, numerical checks and figure generation and are available at `github.com/bradlipovsky/allan-hills-stratigraphy`.

AUTHOR CONTRIBUTIONS

Bradley Paul Lipovsky developed the analysis and wrote the manuscript draft.

COMPETING INTERESTS

None.

ACKNOWLEDGEMENTS

The author received no funding from The Center for Old Ice Exploration (COLDEX), an NSF Science and Technology Center (NSF-2019719), for this work. The author nevertheless benefited from the Center's generous intellectual environment and is grateful for conversations with colleagues across its community.

OpenAI Codex using GPT-5 and `5.6-sol` (available at `openai.com/codex`) was used from 3 August to 1 September 2026 to assist with literature searches, drafting and revising manuscript text, LaTeX formatting, numerical-code development and the search for illustrative model geometries and boundary conditions. The author reviewed and revised all AI-assisted material, verified the cited sources, equations, code and numerical results, and takes full responsibility for the manuscript.

REFERENCES

Alley RB, Gow AJ, Meese DA, Fitzpatrick JJ, Waddington ED and Bolzan JF (1997) Grain-scale processes, folding, and stratigraphic disturbance in the GISP2 ice core. *Journal of Geophysical Research: Oceans*, **102**(C12), 26819–26830 (doi: 10.1029/96JC03836)

Alsop GI and Condon DJ (2025) Shear zone folds: structural analysis and interpretation. *Journal of Structural Geology*, **201**, 105544 (doi: 10.1016/j.jsg.2025.105544)

Bastida F, Aller J, Fernández FJ, Lisle RJ, Bobillo-Ares NC and Menéndez O (2014) Recumbent folds: key structural elements in orogenic belts. *Earth-Science Reviews*, **135**, 162–183 (doi: 10.1016/j.earscirev.2014.05.002)

Bintanja R (1999) On the glaciological, meteorological, and climatological significance of antarctic blue ice areas. *Reviews of Geophysics*, **37**(3), 337–359 (doi: 10.1029/1999RG900007)

Blatter H (1995) Velocity and stress fields in grounded glaciers: a simple algorithm for including deviatoric stress gradients. *Journal of Glaciology*, **41**(138), 333–344 (doi: 10.3189/S002214300001621X)

Bons PD, Jansen D, Mundel F, Bauer CC, Binder T, Eisen O, Jessell MW, Llorens MG, Steinbach F, Steinhage D and Weikusat I (2016) Converging flow and anisotropy cause large-scale folding in greenland's ice sheet. *Nature Communications*, **7**, 11427 (doi: 10.1038/ncomms11427)

Bons PD, Hu Y, Llorens MG, Franke S, Stoll N, Weikusat I, Westhoff J and Zhang Y (2025) Folding due to anisotropy in ice, from drill-core-scale cloudy bands to km-scale internal reflection horizons. *The Cryosphere*, **19**, 5095–5109 (doi: 10.5194/tc-19-5095-2025)

Chung A, Parrenin F, Mulvaney R, Vittuari L, Frezzotti M, Zanutta A, Lilien DA, Cavitte MGP and Eisen O (2025) Age, thinning and spatial origin of the Beyond EPICA ice from a 2.5d ice flow model. *The Cryosphere*, **19**(10), 4125–4140 (doi: 10.5194/tc-19-4125-2025)

Cuffey KM and Paterson WSB (2010) *The Physics of Glaciers*. Elsevier, Amsterdam, 4 edition

Dansgaard W and Johnsen SJ (1969) A flow model and a time scale for the ice core from Camp Century, Greenland. *Journal of Glaciology*, **8**(53), 215–223 (doi: 10.3189/S0022143000031208)

Fazio E, Alsop GI, Nania L, Graziani R, Iaccarino S, Montomoli C, Carosi R, Luzin V, Salvemini F, Gambino S, Cirrincione R and Mamtani MA (2024) CPO and quantitative textural analyses within sheath folds. *Journal of Structural Geology*, **178**, 105000 (doi: 10.1016/j.jsg.2023.105000)

Franke S, Bons PD, Westhoff J, Weikusat I, Binder T, Streng K, Steinhage D, Helm V, Eisen O, Paden JD, Eagles G and Jansen D (2022) Holocene ice-stream shutdown and drainage basin reconfiguration in northeast Greenland. *Nature Geoscience*, **15**(12), 995–1001 (doi: 10.1038/s41561-022-01082-2)

Gudmundsson GH (1997a) Basal-flow characteristics of a linear medium sliding frictionless over small bedrock undulations. *Journal of Glaciology*, **43**(143), 71–79 (doi: 10.3189/S0022143000002823)

Gudmundsson GH (1997b) Basal-flow characteristics of a non-linear flow sliding frictionless over strongly undulating bedrock. *Journal of Glaciology*, **43**(143), 80–89 (doi: 10.3189/S0022143000002835)

Higgins JA, Kurbatov AV, Spaulding NE, Brook EJ, Introne DS, Chimiak LM, Yan Y, Mayewski PA and Bender ML (2015) Atmospheric composition 1 million years ago from blue ice in the allan hills, antarctica. *Proceedings of the National Academy of Sciences*, **112**(22), 6887–6891 (doi: 10.1073/pnas.1420232112)

Hindmarsh RCA, Leysinger Vieli GJMC, Raymond MJ and Gudmundsson GH (2006) Draping or overriding: The effect of horizontal stress gradients on internal layer architecture in ice sheets. *Journal of Geophysical Research: Earth Surface*, **111**(F2), F02018 (doi: 10.1029/2005JF000309)

Hindmarsh RCA, Leysinger Vieli GJMC and Parrenin F (2009) A large-scale numerical model for computing isochrone geometry. *Annals of Glaciology*, **50**(51), 130–140 (doi: 10.3189/172756409789097450)

Holschuh N, Christianson K and Anandakrishnan S (2014) Power loss in dipping internal reflectors, imaged using ice-penetrating radar. *Annals of Glaciology*, **55**(67), 49–56 (doi: 10.3189/2014AoG67A005)

Holschuh N, Christianson K, Dienstfrey W, Hills B, Hoffman AO, Paden J, Winter K and Zuraw R (2026) Entrained debris records regrowth of the Greenland Ice Sheet after the last interglacial. *Nature Geoscience*, **19**(5), 573–580 (doi: 10.1038/s41561-026-01950-1)

Hudleston PJ (1976) Recumbent folding in the base of the Barnes Ice Cap, Baffin Island, Northwest Territories, Canada. *Geological Society of America Bulletin*, **87**(12), 1684–1692 (doi: 10.1130/0016-7606(1976)87<1684:RFITBO>2.0.CO;2)

Izeboud M, Legrain E, Tollenaar V, Pallandre F, Grosrenaud N, Ardoin L, Pattyn F, Blard PH, Gillain MA, Debaille V, Goderis S, Pinto GA, Pourkhorsandi H, Fripiat F and Zekollari H (2026) Initial survey of blue ice areas for the recovery of old ice in the Sør Rondane Mountains (Dronning Maud Land, East Antarctica). *Open Research Europe*, **6**, 17 (doi: 10.12688/openreseurope.21562.2)

Jacobel RW and Bindschadler RA (1993) Radar studies at the mouths of ice streams D and E, Antarctica. *Annals of Glaciology*, **17**, 262–268 (doi: 10.3189/S0260305500012945)

Jacobson HP and Waddington ED (2004) Recumbent folding in ice sheets: a core-referential study. *Journal of Glaciology*, **50**(168), 3–16 (doi: 10.3189/172756504781830204)

Jacobson HP and Waddington ED (2005) Recumbent folding of divide arches in response to unsteady ice-divide migration. *Journal of Glaciology*, **51**(173), 201–209 (doi: 10.3189/172756505781829412)

Jansen D, Franke S, Bauer CC, Binder T, Dahl-Jensen D, Eichler J, Eisen O, Hu Y, Kerch J, Llorens MG, Miller H, Neckel N, Paden J, de Riese T, Sachau T, Stoll N, Weikusat I, Wilhelms F, Zhang Y and Bons PD (2024) Shear margins in upper half of Northeast Greenland Ice Stream were established two millennia ago. *Nature Communications*, **15**(1), 1193 (doi: 10.1038/s41467-024-45021-8)

Kehrl L, Conway H, Holschuh N, Campbell S, Kurbatov AV and Spaulding NE (2018) Evaluating the duration and continuity of potential climate records from the allan hills blue ice area, east antarctica. *Geophysical Research Letters*, **45**(9), 4096–4104 (doi: 10.1029/2018GL077511)

Kirkpatrick LR, Carter AJ, Marks-Peterson J, Shackleton S and Fudge TJ (2025) Three-dimensional multitrack electrical conductivity method for interpretation of complex ice core stratigraphy. *Journal of Glaciology*, **71**, e105 (doi: 10.1017/jog.2025.10081)

Leysinger Vieli GJMC, Martín C, Hindmarsh RCA and Lüthi MP (2018) Basal freeze-on generates complex ice-sheet stratigraphy. *Nature Communications*, **9**, 4669 (doi: 10.1038/s41467-018-07083-3)

Lilien DA, Steinhage D, Taylor D, Parrenin F, Ritz C, Mulvaney R, Martín C, Yan JB, O'Neill C, Frezzotti M, Miller H, Gogineni P, Dahl-Jensen D and Eisen O (2021) Brief communication: New radar constraints support presence of ice older than 1.5 Myr at little dome c. *The Cryosphere*, **15**(4), 1881–1888 (doi: 10.5194/tc-15-1881-2021)

Lipovsky BP (2022) Density matters: ice compressibility and glacier mass estimation. *Journal of Glaciology*, **68**(270), 831

Manos JM, Shaya M, Kirkpatrick L, Stoll N, Banerjee A, Hishamunda V, Horlings AN, Hudak A, Shapero DR, Fudge TJ, Higgins JA, Steig EJ, Brook EJ and Lipovsky BP (2026) Ice flow controls on old ice preservation in the Allan Hills, Antarctica, preprint

Martín C, Gudmundsson GH, Pritchard HD and Gagliardini O (2009) On the effects of anisotropic rheology on ice flow, internal structure, and the age–depth relationship at ice divides. *Journal of Geophysical Research: Earth Surface*, **114**(F4), F04001 (doi: 10.1029/2008JF001204)

Meyer CR and Creyts TT (2017) Formation of ice eddies in subglacial mountain valleys. *Journal of Geophysical Research: Earth Surface*, **122**(9), 1574–1588 (doi: 10.1002/2017JF004329)

Moffatt HK (1964) Viscous and resistive eddies near a sharp corner. *Journal of Fluid Mechanics*, **18**(1), 1–18 (doi: 10.1017/S0022112064000015)

Nabavi ST and Fossen H (2021) Fold geometry and folding—a review. *Earth-Science Reviews*, **222**, 103812 (doi: 10.1016/j.earscirev.2021.103812)

Ng F and King EC (2011) Kinematic waves in polar firn stratigraphy. *Journal of Glaciology*, **57**(206), 1119–1134 (doi: 10.3189/002214311798843340)

Ng F and King EC (2013) Formation of RADARSAT backscatter feature and undulating firn stratigraphy at an ice-stream margin. *Annals of Glaciology*, **54**(64), 90–96 (doi: 10.3189/2013AoG64A202)

Nye JF (1963) Correction factor for accumulation measured by the thickness of the annual layers in an ice sheet. *Journal of Glaciology*, **4**(36), 785–788 (doi: 10.3189/S0022143000028367)

Parrenin F (2013) *Sur l'âge de la glace et des bulles d'air dans les calottes polaires*. Ph.D. thesis, Université Joseph Fourier, Grenoble, France

Parrenin F and Hindmarsh RCA (2007) Influence of a non-uniform velocity field on isochrone geometry along a steady flowline of an ice sheet. *Journal of Glaciology*, **53**(183), 612–622 (doi: 10.3189/002214307784409298)

Parrenin F, Hindmarsh RCA and Rémy F (2006) Analytical solutions for the effect of topography, accumulation rate and lateral flow divergence on isochrone layer geometry. *Journal of Glaciology*, **52**(177), 191–202 (doi: 10.3189/172756506781828728)

Parrenin F, Chung A and Martín C (2025) age_flow_line-1.0: a fast and accurate numerical age model for a pseudo-steady flow tube of an ice sheet. *Geoscientific Model Development*, **18**, 8203–8216 (doi: 10.5194/gmd-18-8203-2025)

Ross N, Corr H and Siegert M (2020) Large-scale englacial folding and deep-ice stratigraphy within the West Antarctic Ice Sheet. *The Cryosphere*, **14**(6), 2103–2114 (doi: 10.5194/tc-14-2103-2020)

Schmalholz SM and Mancktelow NS (2016) Folding and necking across the scales: a review of theoretical and experimental results and their applications. *Solid Earth*, **7**(5), 1417–1465 (doi: 10.5194/se-7-1417-2016)

Schoof C and Hindmarsh RCA (2010) Thin-film flows with wall slip: An asymptotic analysis of higher order glacier flow models. *The Quarterly Journal of Mechanics and Applied Mathematics*, **63**(1), 73–114 (doi: 10.1093/qjmam/hbp025)

Shackleton S, Hishamunda V, Davidge L, Brook EJ, Marks-Peterson J, Carter A, Aarons S, Kurbatov AV, Introne DS, Yan Y, Nesbitt IM, Buizert C, Steig EJ, Schauer AJ, Morgan J, Neff PD, Epifanio JA, Severinghaus JP, Bender ML and Higgins JA (2025) Miocene and pliocene ice and air from the allan hills blue ice area, east antarctica. *Proceedings of the National Academy of Sciences*, **122**(44), e2502681122 (doi: 10.1073/pnas.2502681122)

Spaulding NE, Spikes VB, Hamilton GS, Mayewski PA, Dunbar NW, Harvey RP, Schutt J and Kurbatov AV (2012) Ice motion and mass balance at the allan hills blue-ice area, antarctica, with implications for paleoclimate reconstructions. *Journal of Glaciology*, **58**(208), 399–406 (doi: 10.3189/2012JoG11J176)

Stoll N, Shaya M, Kirkpatrick L, Freitag J, Hishamunda V, Manos JM, Jansen D, Weikusat I, Fegyveresi J, Lipovsky B, Brook EJ, Shackleton S, Higgins JA and Fudge TJ (2026) Fabric, texture, and bubble characteristics of the million-year old allan hills blue ice core ALHIC1901. *Journal of Geophysical Research: Solid Earth*, **131**(5), e2026JB033890 (doi: 10.1029/2026JB033890)

Thorsteinsson T and Waddington ED (2002) Folding in strongly anisotropic layers near ice-sheet centers. *Annals of Glaciology*, **35**, 480–486 (doi: 10.3189/172756402781816708)

Waddington ED (2010) Life, death and afterlife of the extrusion flow theory. *Journal of Glaciology*, **56**(200), 973–996 (doi: 10.3189/002214311796406022)

Waddington ED, Bolzan JF and Alley RB (2001) Potential for stratigraphic folding near ice-sheet centers. *Journal of Glaciology*, **47**(159), 639–648 (doi: 10.3189/172756501781831756)

Whillans IM and Johnsen SJ (1983) Longitudinal variations in glacial flow: theory and test using data from the Byrd Station Strain Network, Antarctica. *Journal of Glaciology*, **29**(101), 78–97 (doi: 10.3189/S0022143000005165)

Wolovick MJ and Creyts TT (2016) Overturned folds in ice sheets: Insights from a kinematic model of traveling sticky patches and comparisons with observations. *Journal of Geophysical Research: Earth Surface*, **121**(5), 1065–1083 (doi: 10.1002/2015JF003698)

Wolovick MJ, Creyts TT, Buck WR and Bell RE (2014) Traveling slippery patches produce thickness-scale folds in ice sheets. *Geophysical Research Letters*, **41**(24), 8895–8901 (doi: 10.1002/2014GL062248)

Yan Y, Bender ML, Brook EJ, Clifford HM, Kemeny PC, Kurbatov AV, Mackay S, Mayewski PA, Ng J, Severinghaus JP and Higgins JA (2019) Two-million-year-old snapshots of atmospheric gases from antarctic ice. *Nature*, **574**, 663–666 (doi: 10.1038/s41586-019-1692-3)

Zhang Y, Sachau T, Franke S, Yang H, Li D, Weikusat I and Bons PD (2024) Formation mechanisms of large-scale folding in greenland's ice sheet. *Geophysical Research Letters*, **51**(16), e2024GL109492 (doi: 10.1029/2024GL109492)

NOTATION

Table 1: Notation. Units are given for the dimensional quantities used in the numerical example; all fluxes are ice-equivalent.

Symbol	Definition	Units
Coordinates and kinematics		
x, z	Horizontal and vertical Cartesian coordinates; x increases downstream.	m
x_0	Horizontal coordinate of surface deposition; a material-origin label.	m
ξ, ζ	Horizontal and vertical coordinates of integration.	m
z_0	Elevation of an unperturbed streamline in the periodic calculation.	m

Table 1 continued

Symbol	Definition	Units
$s(x)$	Free-surface elevation.	m
H, L, ℓ	Ice thickness, horizontal forcing scale and length of a reverse-shear segment.	m
t, τ, T	Time since deposition, stratigraphic age and trajectory duration or orbit period.	yr
$\boldsymbol{u} = [u, w]^{\mathsf{T}}$	Velocity vector and its horizontal and vertical components.	$\mathrm{m\,yr^{-1}}$
u_s, u_{s0}	Horizontal surface speed and its value at deposition.	$\mathrm{m\,yr^{-1}}$
U, U_b	Characteristic horizontal speed and uniform background plug-flow speed.	$\mathrm{m\,yr^{-1}}$
$U_{\min}, U_{\mathrm{dep}}$	Lower speed bound on a trajectory segment and upper bound on speed at deposition.	$\mathrm{m\,yr^{-1}}$
u_1	First-order horizontal-velocity perturbation.	$\mathrm{m\,yr^{-1}}$
$\dot{a}, \dot{a}_0$	Ice-equivalent surface accumulation rate and its value at x_0.	$\mathrm{m\,yr^{-1}}$
ψ, Ψ	Streamfunction per unit width and its restriction to the surface, $\Psi(x) = \psi[x, s(x)]$.	$\mathrm{m^2\,yr^{-1}}$
$\delta x, \delta x_0$	Horizontal separations at observation and deposition.	m
Parrenin–Hindmarsh coordinates		
Q, Q^{ref}	Total horizontal flow-tube flux and its value at a reference position.	$\mathrm{m^3\,yr^{-1}}$
Ω	Streamfunction normalized by total flux.	1
π, θ	Logarithmic flux coordinates: $\pi = \ln[Q(x)/Q^{\mathrm{ref}}]$ and $\theta = \ln \Omega$.	1
π_0	Logarithmic flux coordinate of surface deposition.	1
$\delta\pi, \delta\pi_0$	Neighboring-particle separations in logarithmic flux at observation and deposition.	1
α	Path-sign parameter defined by $\delta\pi = (1-\alpha)\delta\pi_0$.	1
Stratigraphic order		
$\mathcal{J}$	Isochrone-order Jacobian, $\partial x/\partial x_0\|_\tau$.	1
λ_z	Vertical thinning function for ordered stratigraphy.	1
u_z, u_z^+, u_z^-	Vertical shear and its positive and negative parts.	$\mathrm{yr^{-1}}$
$\dot{\gamma}_{\mathrm{rev}}$	Upper bound on reverse vertical shear.	$\mathrm{yr^{-1}}$
$\mathcal{P}, \mathcal{R}$	Accumulated positive-shear and reverse-shear contributions.	1
$\mathcal{B}$	Order budget, $1 + \mathcal{P} - \mathcal{R}$.	1
Stress balance and asymptotic quantities		

Table 1 continued

Symbol	Definition	Units
$p, p_{\mathrm{atm}}, p_{\mathrm{nh}}$	Pressure, atmospheric pressure and nonhydrostatic pressure.	Pa
ρ	Ice density.	$\mathrm{kg\,m^{-3}}$
$\boldsymbol{g}, g$	Gravitational acceleration and its magnitude.	$\mathrm{m\,s^{-2}}$
$\boldsymbol{\tau}$	Deviatoric stress tensor; distinct from scalar age τ.	Pa
$\tau_{xx}, \tau_{xz}, \tau_{xz}^{s}$	Longitudinal stress, shear stress and surface shear stress.	Pa
$\boldsymbol{D}, \eta$	Strain-rate tensor and scalar effective viscosity.	$\mathrm{yr^{-1}}$, $\mathrm{Pa\,yr}$
G, R_{FS}	Gravity-driven and residual full-Stokes contributions to u_z.	$\mathrm{yr^{-1}}$
$\mathcal{G}, \mathcal{F}$	Cumulative gravity-driven and residual full-Stokes order contributions.	1
ε	Glacier aspect ratio H/L.	1
ϵ_b, k	Roughness-amplitude parameter and horizontal wavenumber.	1, $\mathrm{m^{-1}}$
Numerical boundary condition		
$\boldsymbol{\sigma}$	Full Cauchy stress tensor.	Pa
$\boldsymbol{t}, \boldsymbol{n}$	Unit tangent and outward unit normal on the bed.	1
u_t, u_n	Tangential and normal basal velocity components.	$\mathrm{m\,yr^{-1}}$
τ_b, C	Resisting basal shear stress and linear-sliding mobility.	Pa, $\mathrm{m\,yr^{-1}\,Pa^{-1}}$
β	Mean surface slope used to orient gravity in the numerical example.	rad
Operators and conventions		
$(\cdot)_x, (\cdot)_z, (\cdot)_t$	Partial derivatives with respect to x, z, t; u_t instead denotes tangential velocity where explicitly stated.	—
$\mathrm{D}/\mathrm{D}t, \nabla$	Material time derivative and spatial gradient.	—
$(\cdot)^{\mathsf{T}}, \{\cdot, \cdot\}$	Transpose and Poisson bracket.	—
$\partial(\cdot)/\partial x\|_{\psi}$	Partial derivative with the subscripted coordinate held fixed; analogous notation is used for other variables.	—
$[f]_{-}$	Negative-part magnitude, $\max(-f, 0)$.	units of f
$\mathrm{sgn}, \det, O(\cdot)$	Sign, determinant and asymptotic-order notation.	—

RELATIONSHIP TO PREVIOUS STUDIES

Table 2: Relationship between established folding analyses and the present formulation.

Study	Primary question	Diagnostic and scope
Hudleston (1976)	How did observed basal recumbent folds form?	A transient change in flow creates misalignment, followed by passive amplification over an irregular bed.
Whillans and Johnsen (1983)	How do fixed basal variations distort radar layers?	Linear-viscous flow over relief with variable sliding and drag; calculated undulations match Byrd Station radar layers.
Waddington and others (2001)	Does a pre-existing local wrinkle flatten or rotate toward overturning?	Instantaneous tangent slope relative to a steady reference isochrone.
Jacobson and Waddington (2004)	Does a finite-strain history overturn an injected disturbance?	Deformation gradient integrated along trajectories.
Parrenin and others (2006); Parrenin and Hindmarsh (2007)	How does steady flow shape isochrones and preserve particle order?	Log total flux and log normalized stream-function straighten trajectories; the path-sign factor maps deposition coordinate π_0 to present coordinate π.
Ng and King (2011, 2013)	Can steady spatial forcing generate folded firn geometry?	Accumulation and near-surface flow generate single-valued layer undulations, but not recumbent order reversal.
Bons and others (2016); Franke and others (2022)	What do three-dimensional radar surveys show about large folds?	Dated horizons contain overturned and sheath folds that record convergence, basal shear and former flow configurations.
Wolovick and others (2014); Wolovick and Creyts (2016)	Can changing basal traction generate observed overturning?	Traveling slippery or sticky patches produce thickness-scale overturned folds.
Hindmarsh and others (2006)	Do layers drape or override bed and basal-boundary perturbations?	Perturbation and full-mechanical models; wavelength controls architecture.
Zhang and others (2024)	How do anisotropy, convergent flow and bed relief amplify englacial folds?	Full-Stokes growth of active or bed-seeded structures, including recumbent basal folds.
Hindmarsh and others (2009); Parrenin and others (2025)	How can age and thinning be computed accurately in steady flow tubes?	Eulerian and characteristic solvers for age, origin and vertical thinning.
Gudmundsson (1997a)	Can rough-bed Stokes flow contain local extrusion?	Analytical velocity extrema and reverse vertical shear near sinusoidal relief.
This study	Has cumulative reverse shear erased depositional ordering?	Signed inverse-thinning factor, positive–negative shear budget, full-Stokes threshold, obstacle bounds and trajectory diagnostic.

INVERSE-COORDINATE IDENTITIES

Equation 6 can be written

$$\begin{bmatrix} \tau_x & \tau_z \\ \psi_x & \psi_z \end{bmatrix} \begin{bmatrix} \mathrm{d}x \\ \mathrm{d}z \end{bmatrix} = \begin{bmatrix} \mathrm{d}\tau \\ \mathrm{d}\psi \end{bmatrix}, \qquad \det = 1. \tag{A1}$$

The inverse transformation is

$$\begin{bmatrix} \mathrm{d}x \\ \mathrm{d}z \end{bmatrix} = \begin{bmatrix} \psi_z & -\tau_z \\ -\psi_x & \tau_x \end{bmatrix} \begin{bmatrix} \mathrm{d}\tau \\ \mathrm{d}\psi \end{bmatrix} = \begin{bmatrix} u & -\tau_z \\ w & \tau_x \end{bmatrix} \begin{bmatrix} \mathrm{d}\tau \\ \mathrm{d}\psi \end{bmatrix}. \tag{A2}$$

Therefore

$$x_\tau|_\psi = u, \quad z_\tau|_\psi = w, \quad x_\psi|_\tau = -\tau_z, \quad z_\psi|_\tau = \tau_x. \tag{A3}$$

The first two identities state that advancing one unit in age at fixed streamline follows the velocity for one unit of time. The latter two specify the equal-age tangent. Multiplication by $\mathrm{d}\psi/\,\mathrm{d}x_0 = \dot{a}_0$ yields Equation 17 and the corresponding vertical tangent component.

EXTENSION TO STEADY VARIABLE-DENSITY FLOW

Below the firn, glacier ice is commonly approximated as incompressible with nearly constant density (Lipovsky, 2022). The coordinate construction extends to a steady variable-density flow satisfying

$$\nabla \cdot (\rho \boldsymbol{u}) = 0. \tag{A4}$$

Define the mass-flux streamfunction by

$$\rho u = \psi_z, \qquad \rho w = -\psi_x. \tag{A5}$$

Then

$$\begin{vmatrix} \tau_x & \tau_z \\ \psi_x & \psi_z \end{vmatrix} = \rho(u\tau_x + w\tau_z) = \rho. \tag{A6}$$

The mapping remains nonsingular for $\rho > 0$, and the same order interpretation follows after replacing volume flux by mass flux. The constant-density formula therefore extends to positive variable density, with density factors in the cumulative weights.

FIRST-ORDER PERIODIC CANCELLATION ABOUT PLUG FLOW

Let

$$u(x, z; \epsilon_b) = U_b + \epsilon_b u_1(x, z) + O(\epsilon_b^2), \qquad U_b > 0, \tag{A7}$$

where U_b is spatially uniform and u_1 is periodic in x with wavelength $2\pi/k$ and zero horizontal mean at each elevation. Then

$$u_z = \epsilon_b u_{1,z} + O(\epsilon_b^2), \qquad u^{-3} = U_b^{-3} + O(\epsilon_b). \tag{A8}$$

Because the background integrand is identically zero, the $O(\epsilon_b)$ displacement of the trajectory affects the integral only at $O(\epsilon_b^2)$. Evaluating the first-order term along the unperturbed streamline $z = z_0$ gives

$$\int_x^{x+2\pi/k} \frac{u_z}{u^3}\, \mathrm{d}\xi = \frac{\epsilon_b}{U_b^3} \int_x^{x+2\pi/k} u_{1,z}(\xi, z_0)\, \mathrm{d}\xi + O(\epsilon_b^2) = O(\epsilon_b^2), \tag{A9}$$

because differentiation with respect to z preserves the zero horizontal mean of u_1, giving Equation 56. For a vertically sheared background, trajectory displacement can act on the nonzero background integrand at first order, so the cancellation does not follow without additional assumptions.